Controlling the grain orientation during laser powder bed fusion to tailor the magnetic characteristics in a Ni-Fe based soft magnet

Zou, Ji; Gaber, Y.; Voulazeris, G.; Li, S.; Vazquez, L.; Liu, Lei Feng; Yao, M. Y.; Wang, Y. J.; Holynski, M.; Bongs, K.; Attallah, M. M.

Document Version
Peer reviewed version

Link to publication on Research at Birmingham portal

Controlling the grain orientation during Laser Powder Bed Fusion to tailor the magnetic characteristics in a Ni-Fe based soft magnet

Ji Zou[a]*, Y Gaber[a], G Voulazeris[b], S Li[a], L Vazquez[a#], Lei-Feng Liu[a], M-Y Yao[c], Y-J Wang[c], M Holynski[b], K Bongs[b], and MM Attallah[a]*

[a] School of Metallurgy and Materials, University of Birmingham, B15 2TT, Birmingham, United Kingdom
[b] School of Physics and Astronomy, University of Birmingham, B15 2TT, Birmingham, United Kingdom
[c] Key Laboratory of Advanced Structural-Functional Integration Materials & Green Manufacturing Technology, Harbin Institute of Technology, Harbin, 150001, China
[#] Current address: IK4-LORTEK, Technological Centre. Arranomendia kalea 4A, Ordizia 20240, Spain
*Corresponding authors: J.Zou@bham.ac.uk and M.M.Attallah@bham.ac.uk

Abstract

<100> is the favoured crystal growth direction during solidification of cubic metals. However, it is the hard magnetisation axis for Ni-rich soft magnetic materials. In this work, a strategy to enhance the magnetic shielding characteristics of laser powder bed processed soft magnetic alloy (permalloy-80) through the control of the crystallographic texture was developed. The strategy involves initially assessing the influence of the process parameters on the development of the (001) orientation within dense builds, then tilting the build orientation to achieve a crystallographic orientation along the magnetisation soft axis. Using this approach, dense cubic samples with the expected (001) texture were produced, with minimised cracking density. Thereafter, cubic samples tilted to achieve (111) and (110) textures were fabricated, as confirmed by X-ray diffraction and electron backscattered diffraction. Over 200 folds improvement in the magnetic susceptibility was found in the (111) textured build, compared with the (100) oriented build. The paper highlights the possibility to control the grain orientations to achieve improved magnetic properties in the build during laser powder bed processing.

Key words: Laser powder bed fusion; Microstructure; Texture; Magnetic properties; Microcracking.

1. Introduction

Originating from their intrinsic anisotropy, crystalline materials could exhibit directionally dependent physical and mechanical properties, if a preferred crystallographic orientation exists within the grain structure, forming a texture [1-3]. It is feasible at the initial processing stages (e.g. during solidification, as in directional solidification) to design the texture in order

to create enhanced directional properties in a specific direction [4-6]. Although this typically occurs at the expense of reduced properties along other directions, the anisotropic properties can be tailored to enhance the direction-specific performance of a component in the design stage if the performance requirements (e.g. stress distribution or thermal fields) are known [2, 7].

In ferromagnetic materials, the anisotropy in magnetic susceptibility can be controlled through aligning the grains under a moderate magnetic field during high temperature annealing, sintering, or solidification [8]. Even feeble magnetic materials can be textured by employing a strong magnetic field (SMF) over 10 Tesla to align the paramagnetic particles in a well-dispersed suspension during shaping [7, 9]. Nonetheless, the ability of the various processing techniques in tailoring the magnetic susceptibility in 3D is fairly limited, either due to geometrical or processing constrains. For instance, controlling the type of texture on the sample formed under external magnetic field can be rather difficult. In fact, only non-cubic materials with either orientated (00l) or (hk0) planes could be achieved by SMF [7, 9].

Benefiting from the laser induced directional cooling/solidification and the layer-by-layer nature in laser powder bed fusion (LPBF) [10], it is customary to observe a strong texture on the as-fabricated structures along the build direction. Generally speaking, the preferred orientations of LBPF samples could be altered depending on the process parameters [11-12], laser beam intensity profile [13] and the laser scanning strategy [14-15], with the later influencing the movement of the heat flux opposite to which the grains grow. For cubic metals and alloys, the <001> family is the favourable growth direction since the four close-packed {111} planes are symmetrically located around the <001> axes, which requires the longest time to solidify [12]. Consequently, a [100] direction is usually found to be parallel to the longitudinal axis of the columnar grains or along the build direction (i.e. (001) texture) in cubic metallic materials, when they were processed at a suitable heat input range via LPBF. Although the type of texture could theoretically be tailored by alternating the laser scan vectors on different layers [16], tuning the as-fabricated texture is a still a challenging task in LPBF. A precise control of the temperature profile around the melt pool using the process parameters, supported with solidification (grain growth) modelling, is required in order to achieve this.

2

In this paper, a novel strategy to tailor the grain orientation of a soft magnetic material permalloy-80 [17-18] is presented. LPBF processing of Permalloy-80 samples was optimised, creating conditions with different textures. Orientation dependent magnetic properties were achieved through tailoring the build orientation and the process parameters.

2. Experimental

LPBF samples were fabricated using a Concept Laser M2 Cusing system, operated using a 400 W continuous wave fibre laser with a wavelength of 1.064 μm, with a maximum beam speed up to 4 m/s and a fixed focus diameter of ~65 μm. An islands scanning strategy with an island size of 5 mm×5mm was adopted, as illustrated schematically in Figure 1.

Gas atomised permalloy-80 powder (Fig.2), supplied by TLS Technik, (77.33Ni, 16.43Fe, 5.94Mo, 0.03Cu, 0.03Cr, 0.134O and others<0.02, values in wt. %) was used to fabricate 10 × 10 × 10 mm coupons vertically built on a randomly-textured Ni-superalloy substrate using different parameters as listed in Table I, using a 25 μm layer thickness in an argon atmosphere controlled to <100 ppm O_2. For each condition, at least three samples were produced to assess the reproducibility. After an optimum build condition that reduced the structural defects was identified, additional cubes were built, with one or two rotational angles to the substrate to build (110) and (111) tilted cubes.

The as-fabricated samples were sectioned using electrical discharge machining (EDM), parallel to the build (Z) direction, revealing the XY and YZ planes, mounted, ground using SiC paper and diamond suspension, and gradually polished to 0.05 μm oxide finish. The defects within each sample were quantified from the corresponding optical images (Fig.3). For the analysis, a threshold was applied on the images to produce binary images showing only the defects, including both the cracks and the voids. Stereological methods [19] were followed to quantify the void (porosity) area % and cracking density (expressed in mm/mm^2). The density of as-built samples was also measured using the Archimedes' method [20].

Metallographic samples were also etched in Kalling's reagent for ~10 s to examine the melt pool and the detailed microstructure under a JEOL700 Field Emission Gun Scanning Electron Microscope (FEG-SEM) operated at 20 kV. Energy dispersive X-ray spectroscopy (EDS) line scanning was used to assess the chemical inhomogeneity across a typical micro-crack on the

polished surface before etching. The macro-texture of all the as-fabricated samples in the XY and YZ planes was analysed using X-ray diffraction (XRD) using Cu Kα radiation (λ = 0.154056 nm) in a Bruker (D8 Advance) diffractometer. Data was collected between 40 and 80˚ with a step size of 0.02˚. Electron backscattered diffraction (EBSD) was employed to further investigate the grain orientation in the as-fabricated samples, using a FEI Quanta 3D FEG Dual Focused Ion Beam SEM (FIB-SEM) system, operated at 20 kV and a scanning step size 0.9 μm. EBSD maps and pole figures on the XY or YZ-plane of selected samples were collected. For the titled samples, the grain orientation on the original XY plane of the cube was analysed using EBSD. Site-specific FIB sectioning was used to characterise the crack morphology and prepare transmission electron microscope (TEM) specimen from the cracks on the XY plane. The grain orientation and element mapping from the as-FIBed slice was analysed by a scanning transmission electron microscope (STEM, Talos, FEI) operated at 200 kV. The EDS in Talos is an FEI Super-X system consisting of four symmetric designed SDDs (Silicon Drift Detectors) with a solid angle of 0.9 srad, an energy resolution of 136 eV for Mn-Ka and 10 kilo counts per second output.

Polished samples were further observed using a scanning probe microscope (Bruker Dimension Fastscan/Icon). An Atomic Force Microscope (AFM) and a Magnetic Force Microscope (MFM) were employed in combination on the same system to determine the topographical characteristics of the as-fabricated samples and their magnetic domain structures. The MFM images were taken in the lift mode using a standard magnetic etched silicon probe.

Measurement of the magnetic characteristics (coercivity and susceptibility) of the as-fabricated samples was conducted at room temperature, by applying the magnetization axis either along or normal to the building direction (referred to as XY and YZ, respectively) on $10 \times 10 \times 9$ mm coupons using a LakeShore 7300 vibrating sample magnetometer (VSM). A self-demagnetisation correction was conducted before calculating the coercivity (H_c) and magnetic susceptibility from the hysteresis loop [21].

3. Results and Discussion

3.1 Design of Experiments

The permalloy powder had a spherical morphology, yet with some satellites (Fig.2a and b). The average particle size of the permalloy-80 powder was 44 μm, with a D_{10} and D_{90} of 10 and 72 μm (Fig.2c), respectively. Its apparent and tapped densities were measured at 4.57 and 5.40 g/cm^3 respectively, resulting in a Hausner ratio of 1.18 indicating a good flowability [22].

The builds were characterised to assess the degree of consolidation and the impact of the process parameters on the macro-texture development. Since a fixed layer thickness of 25 μm was used for all the samples, a two-dimensional energy density factor (Eq.1), representing the key process variables to give a semi-quantitative estimate of the heat input [23] was chosen to identify the heat input threshold required to achieve maximum consolidation and minimum defects (pores or cracks).

$$E_d = \frac{P}{v \times h}$$ (Eq.1)

where E_d is the energy density (J/mm^2), P is the laser power (Watt), v is the scan speed (mm/s), and h is scan spacing (mm). Specifically, samples built under an energy density of 1.36 and 4.89 J/mm^2 are referred thereafter as LE (low energy) and HE (high energy) for simplicity (Table I).

Build conditions with E_d<1 J/mm^2 failed to build. A sharp decrease of porosity area % was observed reducing from 15% to 2% when using E_d between 1 and 2 J/mm^2 (Fig.4). Previous work found that the threshold for consolidation in Ni-rich alloys was ~1.5-2 J/mm^2 [23-25], which agrees with the range identified for permalloy-80; being a Ni-rich alloy. On further increasing E_d to 9 J/mm^2, the porosity area % remains at a low level of 0.5-2%, nevertheless it shows a large scatter with the increase in E_d, rather than a clear trend. The porosity area % increased again when the E_d exceeded 9 J/mm^2, possibly due to evaporation/keyhole at high energy density levels. There was no noticeable difference in the porosity area % between the measured porosity on either the XY or YZ planes in the as-fabricated condition. Conversely, the cracking density on the YZ-plane slightly reduced to ~5 mm/mm^2 in the samples built using E_d > ~4 J/mm^2, with the cracking density fluctuating around ~9 mm/mm^2 below 4 J/mm^2. Unlike the density, the cracking density value is much larger on XY plane, especially when E_d is below ~4 J/mm^2, indicating the 2D nature of the crack morphology.

3.2 Cracking formation mechanism

5

The morphology of the defects in the builds varied with the laser energy density (Fig.3). Voids, in half-crescent shape, could be found in the samples built using a low energy density (3a and b). These voids were bent towards the building direction and elongated slightly in the Y-direction; its formation mechanism will be discussed in section 3.3. Meanwhile, keyholes with spherical pores were entrapped in the build structure and could easily be identified when the E_d is too high (3e). It should be noted that cracks exist in all the samples regardless of the E_d levels. In the optimum conditions (3c and 3d), only cracking could be observed, with the pores being totally absent.

According to the differences in the morphologies, two types of cracks could be identified from Fig.3c. Type I crack, which dominates in the defects arrowed in Fig.3c, generally propagated and aligned towards the building direction (Z-axis in Fig.1). Similar micro-cracks have been reported in many LPBF fabricated Ni based alloys [14, 26-28]. Its formation has been previously associated with the thermal residual stress and reduction in ductility in the as-LPBFed part [25, 28]. The thermal residual stresses are generated due to the differences in the elastic and thermal properties between the solidified layers (N) and the molten layers (N+1) (Fig.1) during cooling. The susceptibility to initiate micro-cracking along the grain boundaries was also associated with the segregation of specific alloying elements (e.g. Si and Mn in Hastelloy X [27], or Zr in IN738 [29]) along the grain boundaries. Tomus *et al.* hypothesized that segregation could result in some weakened/brittle phases along the grain boundaries [27]. However, from the EDS line scan on the same alloy manufactured by LPBF, no substantial variation in these elements could be detected from his work [26]. The composition change across a typical crack interface on the HE condition was also measured (Fig.5a and b), only showing a drop in all the elements near the crack tip, which is expected due to the gap along the crack interface. Apart from that, Ni, Fe, Mo, Cr and O were distributed evenly according to the EDS line scan (Fig. 5b) in this work. A slice-and-view on type I crack confirms its 2D nature (Fig.5c). Although nothing appears on the line scan inspection, from the gap in the cracks, fine particles with bright contrast were found to cover the crack surface, while phase with darker contrast could be identified in the area near the polishing surface (5c). However, analysing their compositions using SEM/EDS was difficult since most of the X-ray excitation from these grains could be blocked by the contour of the FIB cutting region, with the EDS pattern always containing contaminations from sputtered Gallium.

6

For this reason, a typical section area for Type I crack was lifted out for a further TEM study. As shown in Fig.6a, the two grains adjacent to the crack have different orientations, meaning that the crack exists along the grain boundary. An array of particles with size smaller than 300 nm was found alongside the grain boundary; they are crystalline according to the corresponding diffraction patterns (Fig.6a). For their compositions, these particles contained oxygen while the other elements are the same as the matrix, as confirmed from the mappings shown in Fig.6b. The quantitative analysis results an averaged oxygen content of ~5 wt% in these particles. This is similar to the observations of Wang *et al.*, who also found oxygen-rich particles along the dendritic cell boundaries in Ni-superalloys processed by LPBF, combined with a significant dislocation activity around them [30]. Those particles were also Ti, Hf, and Ta-rich, which all have high oxygen affinity and solubility limits. These particles, being located at the grain boundary, will result in extra coherency strains (as demonstrated by the dislocation activity), which in addition to the thermal expansion coefficient mismatch and the thermal stresses, might facilitate the crack opening.

Type II cracks are generally randomly oriented, showing a zigzag morphology (circled in Fig.3c and Fig.7). The inner part of the crack could be pulled out during polishing occasionally, leaving a typical dendrite structures surrounded by the crack (7b and 7c); a typical feature of solidification cracking. It can be concluded that the crack formation mechanisms are directly related to the composition of the alloy and their solidification behaviours, as influenced by the process parameters. Although optimising the process parameters could reduce the cracking density, full elimination of cracking can be very challenging in this alloy. The use of hot isostatic pressing to seal these cracks is going to be assessed in future work.

3.3 Crystallographic texture development

XRD patterns from starting permalloy powders, XY and YZ planes of HE are displayed in Fig.8a. Peaks belonging to permalloy-80 were detected in the powder and the corresponding builds, indicating the presence of a single phase. The patterns show no detectable amounts of intermetallics or mixed elemental phases due to the use of a pre-alloyed powder and the rapid cooling associated with the process, which differs from the previous investigations in the literature that used elemental powder blends [31-33]. In the powder, the (111) peak intensity ($I_{(111)}$) is higher than that of (002) peak, which fits well with the standard diffraction pattern

for the FCC phase, where $I_{(002)}/I_{(111)}=0.42$ (JCPDF 04-003-2245). However, $I_{(002)}$ becomes stronger than $I_{(111)}$ in the builds, confirming the favourable (001) solidification texture that formed during LPBF. Interestingly, by plotting the energy density versus the $I_{(002)}/I_{(111)}$ ratio, it was found that the maximum $I_{(002)}/I_{(111)}$ corresponds to a E_d value of 4.89 J/mm^2 (Fig.8b), which coincides with the threshold for getting a low cracking density in the build (Fig.4). Therefore, a condition with a high density, a low cracking density, and a strong (001) texture could be obtained at the same time. It is also clear that the E_d dependence of texture in the YZ plane follows a similar trend as that on XY plane, although the $I_{(002)}/I_{(111)}$ on the XY plane is obviously higher than that in YZ plane over the whole E_d range (Fig.8b).

EBSD mapping revealed the presence of a weak (100) texture in the build performed with E_d of 1.36 J/mm^2 (Fig. 8c, 8e), which increased in the build performed with energy density of 4.89 J/mm^2 (Fig. 8d, 8f). Since the laser scanning vectors are normal to each other in the adjacent islands, the front and side contour of the melt pool could be seen periodically on the etched surface, as highlighted in Fig.8f. Instead of a deep, slightly overlapped, and continuous melt pool (as observed in HE sample), a wide and shallow melt pool was observed in LE, also demonstrating lack of fusion defects. Lack of fusion defects is usually associated with insufficient E_d [23]. Due to the nature of the process, columnar grains are normally dominant in the microstructure, forming towards the melt pool along the building direction. Any discontinuity in the melt pool, as in LE, is likely to interrupt the grain alignment along the (001) direction, inhibiting the continued nucleation of grains from the pre-existing (001) in the previously solidified layers, resulting in a relatively weaker texture and less columnar grains (S1).

The (001) pole figure for the HE sample in Fig.8d confirms that although there is a slight misalignment, a strong (001) texture exists nearly parallel to the three X, Y and Z directions. The role of the slight misalignment between <001> orientations and the build direction (Z-axis) will be discussed later.

In an extreme condition when the E_d is too high (> 9 J/mm^2, e.g. as in Fig. 2e), significant evaporation happens in the melt pool by keyholing, leading to the formation of pores. The presence of the pores will also cause the distortion of the columnar grain structure, and thus resulting in a weaker (001) texture (Fig.8b). The excessive energy input also promoted the formation of cracks and possibly some grain misalignment due to the high residual stresses. In

8

view of that, the $I_{(002)}/I_{(111)}$ ratio was found to reach a maximum point at the peak of consolidation over the investigated range E_d range, only to start reducing as the energy input becomes excessive, resulting in defects as shown in Fig.8b.

3.4 The change of coercivity in the builds

With regards to the magnetic properties, the measured coercivity (H_c) in the builds was found to decrease with the increase in sample density and energy density (Fig.9a). Microstructural features and structural defects, in terms of grain boundaries, pores, and cracks are known to retard the rotation or movement of the magnetic domains [32-33]. As a result, H_c becomes smaller when a denser sample with a lower level of pore and cracking density was achieved. It should be noted that the H_c value of permalloy-80 (76A/m for HE, built under the optimised condition) printed in the present study is much lower than that reported in the literature in additively manufactured permalloy-80 (~400-7957A/m) [34-35], benefiting from a careful design of experiment and the use of pre-alloyed powder, which significantly reduced the amounts of defects in the built. Fig.9a showed that the coercivity values are anisotropic. Moreover, the difference seems to become larger especially at a high E_d level, reflecting the magnetocrystalline anisotropy originating from the stronger texture in the denser samples (e.g. HE), although the magnetocrystalline anisotropy of conventionally processed permalloy-80 is known to be small. On the other hand, further increase the E_d from ~3 J/mm^2 to ~5 J/mm^2 resulted in an increase in density of the sample, i.e. from 8.5 to 8.7 g/cm^3 but has a little influence on the H_c values, which contradicts the view that further densification should result in a reduction in H_c, since magnetocrystalline anisotropy dominates in this range.

3.5 The observation of magnetic domains

AFM topography images show a columnar grain in the HE sample (Fig.9b). After a final polishing by nanosized oxide suspensions, the averaged surface roughness (R_a) of HE and LE measured by AFM was 2.13nm and 3.05 nm. Although their porosity area % values are different, similar R_a values are acquired due to the choice of a dense area for both measurements. The domain structure of LPBF-processed alloys has rarely been investigated. From the MFM images (Fig.9c), domains with an array of alternating contrast are clearly recognised in HE (observed at the same area as that in Fig. 9b), even passing through a grain boundary as arrowed in Fig. 9b&c. This is a typical characteristic for stripe domains (SDs).

SDs have been reported in various materials, including permalloy-80 and Cobalt films [36-37]. The average domain width obtained from Fast Fourier transform (FFT) of these patterns was 1.5 and 1.7 μm for HE and LE, respectively (S2). Again, the E_d has a little influence on the value. As to the direction of the stripe domains, an angle of ~49° between the SDs alignment and grain elongation direction was measured (Fig.9c and S3). Assuming [001] is the direction for the dendritic grain growth during solidification, 49° is close to the angle (54.7°) between [001] and [111] in a FCC metal. This suggests that in the demagnetisation status, SDs in HE prefer aligning along the [111] axis. Likewise, a similar angle was also determined on LE (S4). The magnetic anisotropy (F_k) of a cubic system could be written in Eq. 2:

$$F_k = K_0 + K_1(\alpha_1^2\alpha_2^2 + \alpha_2^2\alpha_3^2 + \alpha_3^2\alpha_1^2) + K_2\alpha_1^2\alpha_2^2\alpha_3^2 \quad \text{(Eq.2)}$$

Where α_1, α_2, α_3 represent the direction cosines of magnetisation and K_0, K_1, K_2 are the anisotropy constants. For permalloy-80, K_1 is -300 J/m^3 and K_2 is negligible [38]. The negative value of K_1 indicates the [111] axis is the easy axis, in line with the findings from MFM observation (Fig.9c). Based on Fig.8 and Fig.9, denser samples exhibit a stronger (100) texture degree. Due to the strong (100) texture, when a magnetic field was applied on the sample, more SDs need to be rotated in the denser samples from an easier axis of [111] to a hard axis of [001] before the motion of the domain walls starts. Such extra step substantially reduces the "softness" of the material by increasing its coercivity field level, which is ascribe to cause the unchanged H_c values with a density increase from 8.5 to 8.7g/cm^3 (Fig.9a), as previously discussed.

3.6 New crystallographic orientation from tilting the (001) texture

Obviously, using the conventional LPBF strategy, at some point, there is a trade-off in the as-fabricated permalloy between the high density/strong (001) texture and the occurrence of a high coercivity value (H_c). The problem was generated because <111> rather than <001> is the easy axis for the magnetisation in permalloy-80, while (001) texture is the dominated feature on LPBF-processed cubic materials and alloys (Fig.10a and d). In a cubic-shaped sample, if the cube was cut along its bulk diagonal line, in view that a cubic texture exists in the sample, (111) texture will dominate on the fresh cut surface. Alternatively, if the cube could be rotated to make its [110] direction perpendicular to the building substrate, apart from two parallel surfaces with (100) texture, the other four should be dominated by (110) texture (Fig.10b and e). Likewise, further tilting the cube to allow its [111] direction to be parallel to

the building direction, all the six surfaces on the orientated cube should display a strong (111) texture. On the analogy of this, the cubes with a prescribed texturisation could be designed. The assumption was further validated by printing cubes with different titling angles to the substrate, when necessary, with some proper support structures as shown in Fig.10. In theory, samples with fully (110) and (111) textured surfaces should be realised in this way. Although the intensity of (220) and (111) peaks in (110) and (111) tilted samples are strong, according to the corresponding XRD patterns (Fig.11a), some minor peaks from the other reflections could still be detected on surfaces of (110) and (111) textured samples, possibly due to the use of the island scanning strategy in LPBF. Some grains with unexpected orientation from their surfaces are also identifiable from the EBSD maps (Fig.10e and f). During LPBF, a series of phenomena including powder spatter, melting/re-melting, selective elemental evaporation and solidification might occur simultaneously when the powder is irradiated by the laser beam. Also, since heat transfer will also occur from the sides of the part being built and not just through the bottom via the substrate, columnar grains do not necessarily grow vertically to the substrate, as marked from S3 and ascertained in the previous work [25]. This might be manifested in a misalignment of the cube texture as previously discussed (Fig.8d). In this work, orientated cubes in Fig.10b and c inherited such misalignment and caused the appearance of grains with unexpected orientations on the surfaces of (110) and (111) textured samples.

As a soft magnetic material, very narrow hysteresis loops were obtained for the all the builds (Fig.11b). It is clearly recognised from these loops (Fig.11b) that manipulating the grain orientation during LPBF could effectively tailor the magnetic properties on the as-fabricated sample, although permalloy-80 is characterised by a low magnetocrystalline anisotropy. Cubes with (111) textured surfaces exhibit a much higher saturation magnetisation and lower H_c field (11b). The Hc was reduced from 76A/m from conventional (001) build for HE to 35A/m for the (111)-tilted/textured sample. More importantly, the initial relative magnetic susceptibility (1000 at a magnetic field of 60A/m) for (111)-tilted/textured sample was over 200 times higher than the one conventionally built with the standard (100) orientation.

Although a remarkable reduction of Hc was obtained in this work compared with the similar materials fabricated by additive manufacturing [31-32], the Hc value here is still much higher than that for commercial permalloy-80, which is between 0.4 and 2.4A/m. It is likely that post-LPBF a heat treatment or hot isostatic pressing is going to be applied to the builds to

further reduce the cracking density and the residual stress. When annealed in a magnetic field in hydrogen atmosphere, the magnetic permeability of permalloy-80 has been reported to increase significantly [18, 39]. Also, considering the cubes investigated currently are still not fully (110) or (111) textured, there are still some spaces to further improve their magnetic properties. With a better control on the laser scan strategies and build orientation during LPBF, or by using a single crystal substrate to form strongly textured builds through epitaxial growth (as previously used in the scanning laser epitaxy process [40]), (111) textured builds with a lower H_c value and higher magnetic susceptibility are likely to be achieved. By combining the aforementioned strategies with the approach proposed in this paper, more obvious directional magnetic properties can be achieved in the LPBFed builds with intrinsically larger magnetocrystalline anisotropy constants.

4. Conclusion

A new strategy to manipulate the grain orientation on LPBFed permalloy-80 was presented in this study. Some key findings of this work can be drawn as follows:

1. A single FCC phase permalloy-80 with porosity <0.5% and cracking density <5mm/mm^2 could be fabricated by LPBF under a high energy density between 4-9 J/mm^2. The best condition to obtain a cube texture is at an E_d of 4.89 J/mm^2.

2. Two types of micro-cracks were identified in the optimum build conditions. Along the YZ plane, Type I propagates along the building direction, with no elemental segregation across the crack. Fine particles with ~5 wt% oxygen were found in the crack gap lifted-out using FIB. These particles might facilitate the crack opening under residual tensile thermal stress. Type II shows a zig-zag profile where the dendrites were found from the crack boundary, which is a typical feature in liquid-state (solidification) cracking.

3. (100) texture in the as-fabricated cube is firstly enhanced by an initial increase in energy density up to 4.89 J/mm^2. Further increasing the E_d deteriorates the texture degree. Poor (100) texture was found on the sample fabricated at a lower E_d due to the voids generated by a "lack of fusion", which hindered the continuity of the melt pool.

4. Typical stripe domains are revealed by MFM on the as-fabricated permalloy-80. SDs could extend through the grain boundary and align to the <111> direction, the easy axis of permalloy. E_d has nearly no effects on the shape and width of the domains

under demagnetization status. The rotation of SDs in (001) textured permalloy may cause a H_c field increase.

5. (110) and (111) textured permalloy-80 could be fabricated by tilting the cubes to allow its [110] and [111] axis normal to the building plane. Although (110) and (111) textures are enhanced in the as-LPBFed samples, the cubes still contains some grains with the other orientations.

6. (111) textured permalloy-80 exhibits fascinating magnetic properties, including low H_c field (~35 A/m) and relatively high magnetic susceptibility up to ~1000 under a magnetic field of 60 A/m.

References

[1] Ozcan AS, Jordan-Sweet J, Stach EA, Tersoff J, Ross FM and Lavoie C, An off-normal fibre-like texture in thin films on single-crystal substrates, Nature 426(2003) 641-645.

[2] C. Corentin, T. Eial, D.R. Koen, S. Yair, V. H. Martin, Combinatorial design of textured mechanical metamaterials, Nature 535(2016) 529–532.

[3] L.F. Hortense, B. Florian, N. Tobias and S. Andre R., Magnetically assisted slip casting of bioinspired heterogeneous composites, Nature Materials 14(2015)1172–1179.

[4] Haxhimali T, Karma A, Gonzales F, and Rappaz M., Orientation selection in dendritic evolution, Nature Materials 5(2006) 660-664.

[5] M. Tane, T. Mayama, A. Oda and H. Nakajima, Effect of crystallographic texture on mechanical properties in porous magnesium with oriented cylindrical pores, Acta Materialia 84(2015) 80-94.

[6] Leifeng Liu, Qingqing Ding, Yuan Zhong, Ji Zou, Jing Wu , Yu-Lung Chiu , Jixue Li , Ze Zhang , Qian Yu and Zhijian Shen. 3D dislocation network in additive manufactured steel breaks strength-ductility trade-off, Materials Today 21(2018) 354-361.

[7] C. F. Hu, Y. Sakka, S. Grasso, T. Nishimura, S. Q. Guo and H. Tanaka, Shell-like Nanolayered Nb_4AlC_3 Ceramic with High Strength and Toughness, Scripta Mater. 64(2011)

765-8.

[8] Y.D. Zhang, C. Esling, J.S. Lecomte, C.S. He, X. Zhao and L. Zuo, Grain boundary characteristics and texture formation in a medium carbon steel during its austenitic decomposition in a high magnetic field, Acta Materialia 53 (2005) 5213–5221.

[9] De-Wei Ni, Guo-Jun Zhang, Yan-Mei Kan and Yoshio Sakka. Highly textured ZrB_2-based ultrahigh temperature ceramics via strong magnetic field alignment, Scripta Mater. 60(2009) 615-618.

[10] Standard Terminology for Additive Manufacturing Technologies, ASTM F2792-12a.

[11] Xin Zhou, Kailun Li, Dandan Zhang, Xihe Liu, Jing Ma, Wei Liu and Zhijian Shen, Textures formed in a CoCrMo alloy by selective laser melting, Journal of Alloys and Compounds 631(2015) 153-164.

[12] Collins, P. C., Brice, D. A., Samimi, P., Ghamarian, I. & Fraser, H. L. Microstructural control of additively manufactured metallic materials, Annu. Rev. Mater. Res. 46(2016) 63–91.

[13] Tien T. Roehling, Sheldon S.Q. Wu, Saad A. Khairallah, John D. Roehling, S. Stefan Soezeri, Michael F. Crumb, Manyalibo J. Matthews, Modulating laser intensity profile ellipticity for microstructural control during metal additive manufacturing, Acta Materialia 128(2017) 197-206.

[14] Luke N Carter, Christopher Martin, Philip J Withers and Moataz M Attallah, The influence of the laser scan strategy on grain structure and cracking behaviour in SLM powder-bed fabricated nickel superalloy, Journal of Alloys and Compounds 615(2014) 338-347.

[15] Fabian Geiger, Karsten Kunze and Thomas Etter, Tailoring the texture of IN738LC processed by selective laser melting (SLM) by specific scanning strategies. Materials Science and Engineering: A 661(2016) 240-246.

[16] V.A. Popovich, E.V. Borisov, A.A. Popovich, V.Sh. Sufiiarov, D.V. Masaylo, L. Alzina, Functionally graded Inconel 718 processed by additive manufacturing: Crystallographic texture, anisotropy of microstructure and mechanical properties, Materials & Design 114 (2017) 441-449.

[17] H.D. Arnold, G.W. Elmen, Permalloy, a new magnetic material of very high permeability, Bell Syst. Tech. J. 2 (1923) 101-111.

[18] "Supermalloy": a New Magnetic Alloy, Nature 161(1948) 554.

[19] Selective laser melting of AlSi10Mg alloy: Process optimisation and mechanical properties development, N Read, W Wang, K Essa, MM Attallah, Materials & Design 65(2015) 417-424.

[20] Standard Test Methods for Density of Compacted or Sintered Powder Metallurgy (PM) Products Using Archimedes' Principle, ASTM B962 – 17.

[21] W.W. Guo, M.C. Dentith, Z.X. Li and C. McA. Powell. Self-demagnetisation corrections in magnetic modelling: some examples, Exploration Geophysics 29(1998) 396-401.

[21] R.O. Grey and J.K. Beddow, On the Hausner Ratio and its relationship to some properties of metal powders, Powder Technology 2(1969) 323-326.

[23] L.N. Carter , X. Wang , N. Read , R. Khan , M. Aristizabal , K. Essa , M.M. Attallah , Process optimisation of selective laser melting using energy density model for nickel based superalloys, Mater. Sci. Technol. 32(2015) 657-661.

[24] Chunlei Qiu, Nicholas J.E. Adkins, Moataz M. Attallah, Selective laser melting of Invar 36: Microstructure and properties, Acta Materialia 103(2016) 382-395.

[25] Moataz M. Attallah, Rachel Jennings, Xiqian Wang and Luke N. Carter, Additive manufacturing of Ni-based superalloys: The outstanding issues, MRS Bulletin 41(2016)758-764.

[26] Neil J. Harrison, Iain Todd, Kamran Mumtaz, Reduction of micro-cracking in nickel superalloys processed by Selective Laser Melting: A fundamental alloy design approach, Acta Materialia, 94(2015) 59-68.

[27] Tomus, D., Jarvis, T., Wu, X., Mei, J., Rometsch, P. and Herny, E, Controlling the microstructure of Hastelloy-X components manufactured by selective laser melting, Phys. Proc., 41 (2013) 816-820.

[28] P. Mercelis, J. P. Kruth, Residual stresses in selective laser sintering and selective laser melting, Rapid Prototyping J., 12 (2006) 254-265.

[29] Michael Cloots, Peter J. Uggowitzer, Konrad Wegener, Investigations on the microstructure and crack formation of IN738LC samples processed by selective laser melting using Gaussian and doughnut profiles, Materials & Design, 89(2016) 770-784.

[30] Xiqian Wang, Luke N. Carter, Bo Pang, Moataz M. Attallah, Michael H. Loretto,

Microstructure and yield strength of SLM-fabricated CM247LC Ni-Superalloy, Acta Materialia, 128(2017)87-95.

[31] Baicheng Zhang, Nour-Eddine Fenineche, Hanlin Liao and Christian Coddet, Microstructure and Magnetic Properties of Fe–Ni Alloy Fabricated by Selective Laser Melting Fe/Ni Mixed Powders, Journal of Materials Science & Technology 29(2013)757-760.

[32] Baicheng Zhang, Nour-Eddine Fenineche, Lin Zhu, Hanlin Liao, Christian Coddet, Studies of magnetic properties of permalloy (Fe–30%Ni) prepared by SLM technology, Journal of Magnetism and Magnetic Materials 324 (2012) 495–500.

[33] Shishkovsky and V.Saphronov, Peculiarities of selective laser melting process for permalloy powder, Materials Letters 171(2016) 208-211.

[34] C.V. Mikler, V. Chaudhary, T. Borkar, V. Soni, D. Choudhuri, R.V. Ramanujan, R. Banerjee, Laser additive processing of Ni-Fe-V and Ni-Fe-Mo Permalloys: Microstructure and magnetic properties, Materials Letters 192(2017) 9-11.

[35] Baicheng Zhang, Nour-Eddine Fenineche, Hanlin Liao, Christian Coddet, Magnetic properties of in-situ synthesized FeNi3 by selective laser melting Fe-80%Ni powders, Journal of Magnetism and Magnetic Materials 336(2013) 49-54.

[36] N. Amos, R. Fernandez, R. Ikkawi, B. Lee, A. Lavrenov, A. Krichevsky, D. Litvinov, and S. Khizroev. Magnetic force microscopy study of magnetic stripe domains in sputter deposited Permalloy thin films, Journal of Applied Physics, 103(2008) 10.1063/1.2835441.

[37] C.T. Hsieh, J.Q. Liu, J.T. Lue, Magnetic force microscopy studies of domain walls in nickel and cobalt films, Applied Surface Science 252 (2005) 1899–1909.

[38] Robert C. O' Handley, Modern Magnetic Materials: Principles and Applications, first ed., John Wiley & Sons, Inc., New York, 2000.

[39] B. LEWIS, The permalloy problem and magnetic annealing in bulk nickel-iron alloys, British Journal of Applied Physics 15(1964) 407-412.

[40] Amrita Basak and Suman Das, Epitaxy and Microstructure Evolution in Metal Additive Manufacturing, Annual Review of Materials Research 46(2016) 125-149.

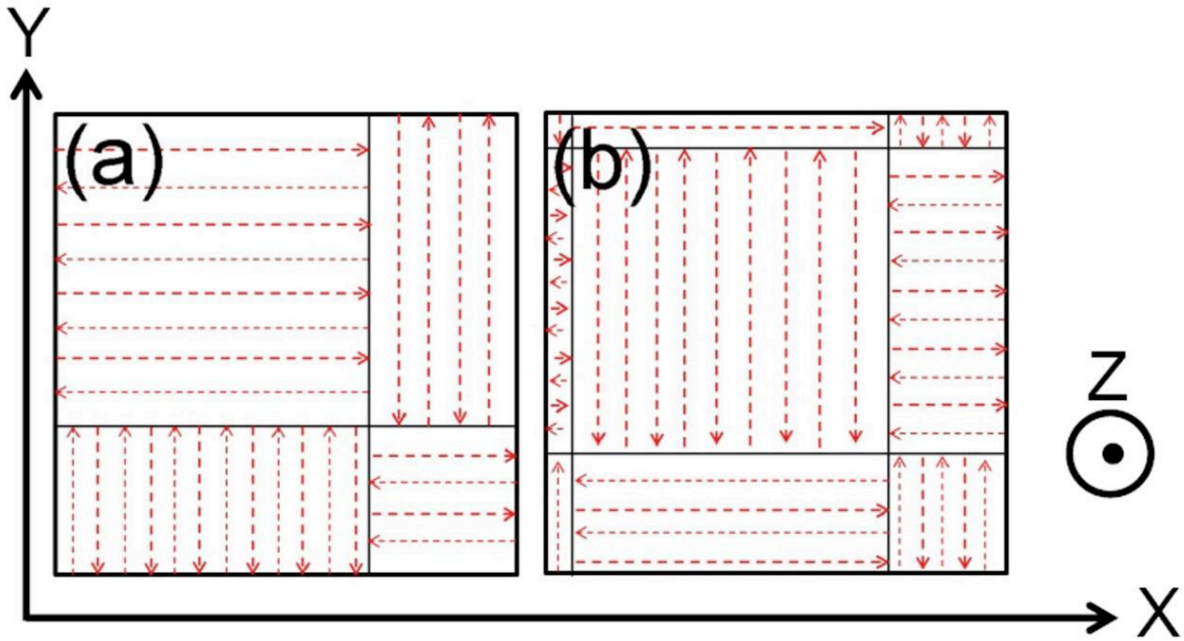**Figure and Table captions**

Figure captions

Figure 1: Schematic diagrams (a and b) with the coordinate axes for LPBF, showing the building direction (Z) and laser scanning strategy used in this work. The alternating laser scanning vectors on N layer and N+1 layer are presented in 1a and 1b.
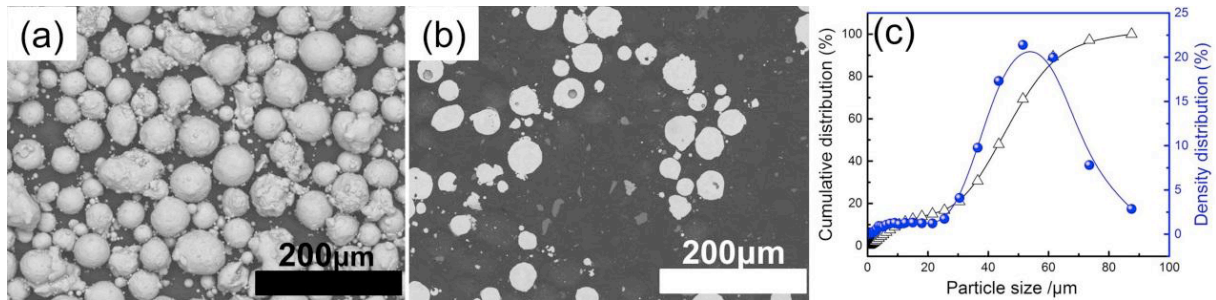

Figure 2: The particle size and distribution of the starting permalloy powder. 2a and 2b are the SEM image of the morphology and polished surface of raw permalloy-80 powder observed by SEM. The corresponding size distribution of the powders is plotted in 2c.
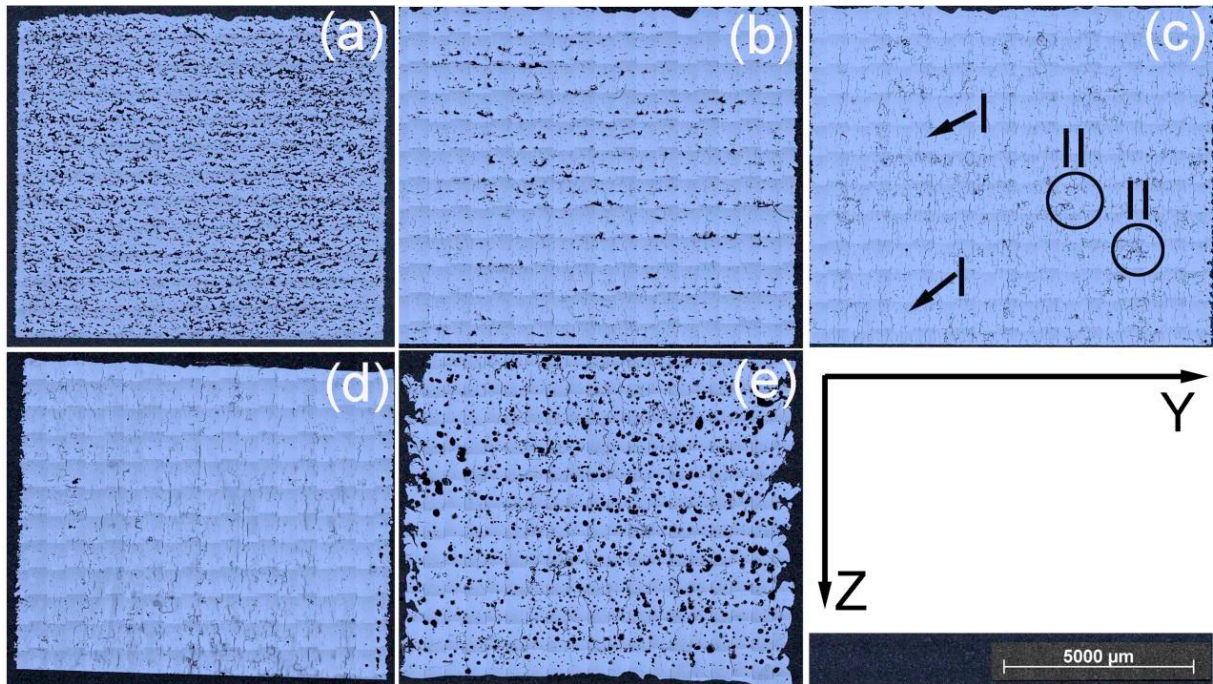
Figure 3: The optical images on the YZ plane permalloy-80 built with increasing energy densities (a-e). The building direction is arrowed. The E_d values adopted from 3a to 3e are 1.19, 2.51, 3.25, 9.03 and 41.67, *cf.* Table I, respectively. In Fig.3c, two types of cracks were identified: type I was arrowed while type II was circled.
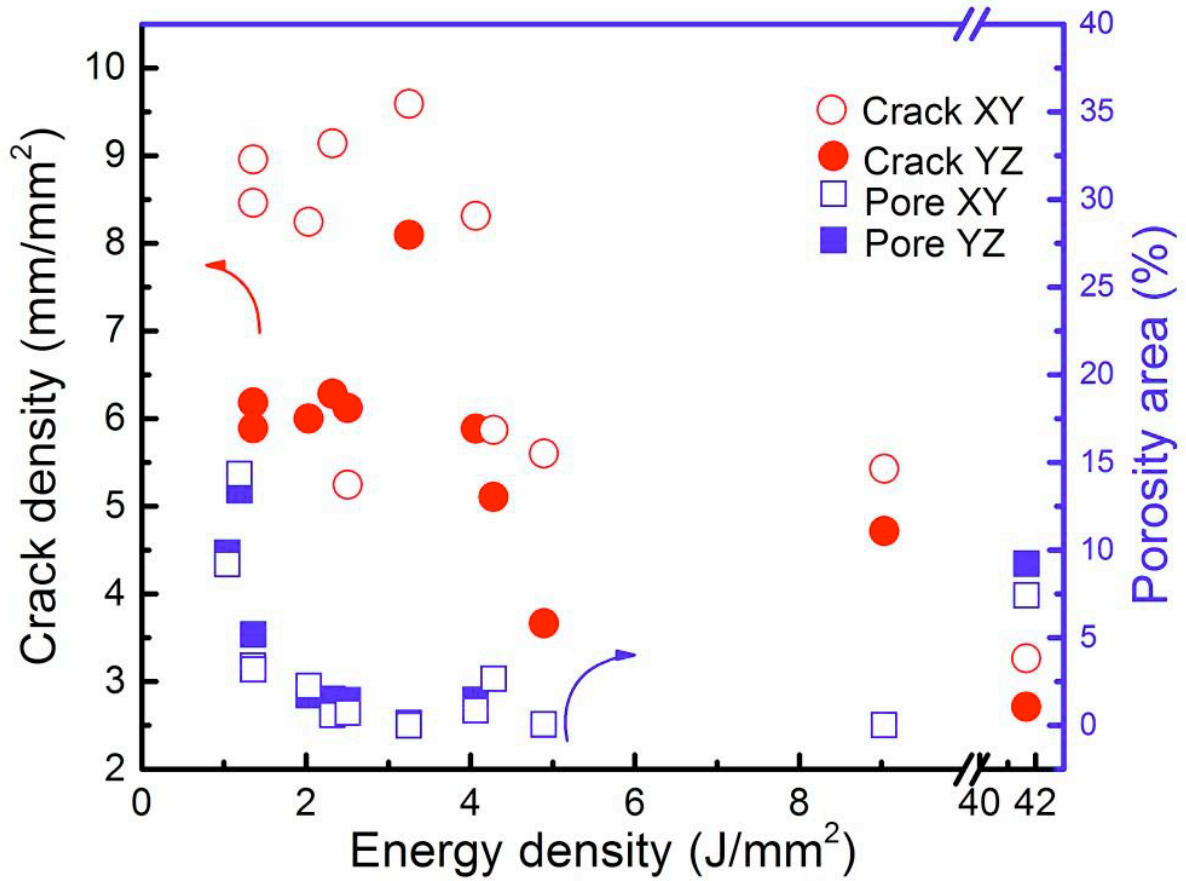
Figure 4: The influence of laser energy density on the cracking density and porosity of as-fabricated samples.
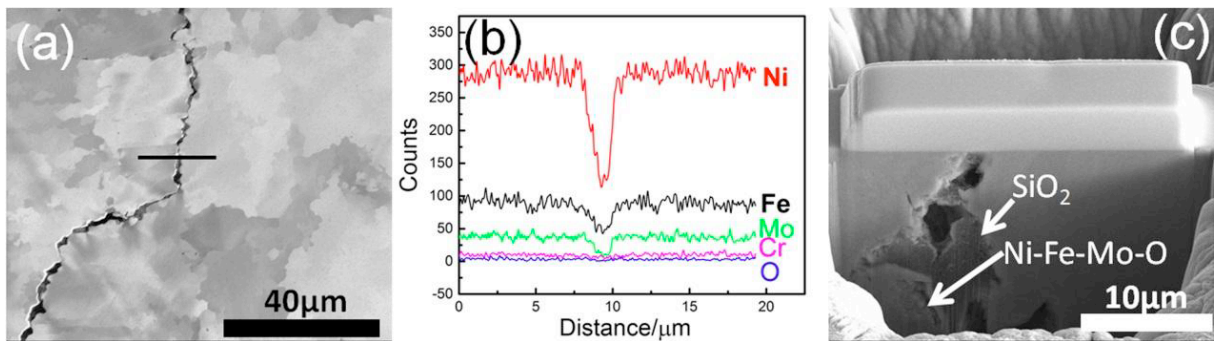
Figure 5: A typical micro-crack on the XY plane of sample HE (5a) built at an E_d of 4.89J/mm^2 (Table I). The composition variation across the crack is shown in the EDS line scan (5b). A side view of the crack was shown in 5c. Extra phases, SiO$_2$, from the polishing media and Ni-Fe-Mo-O were marked in 5c.
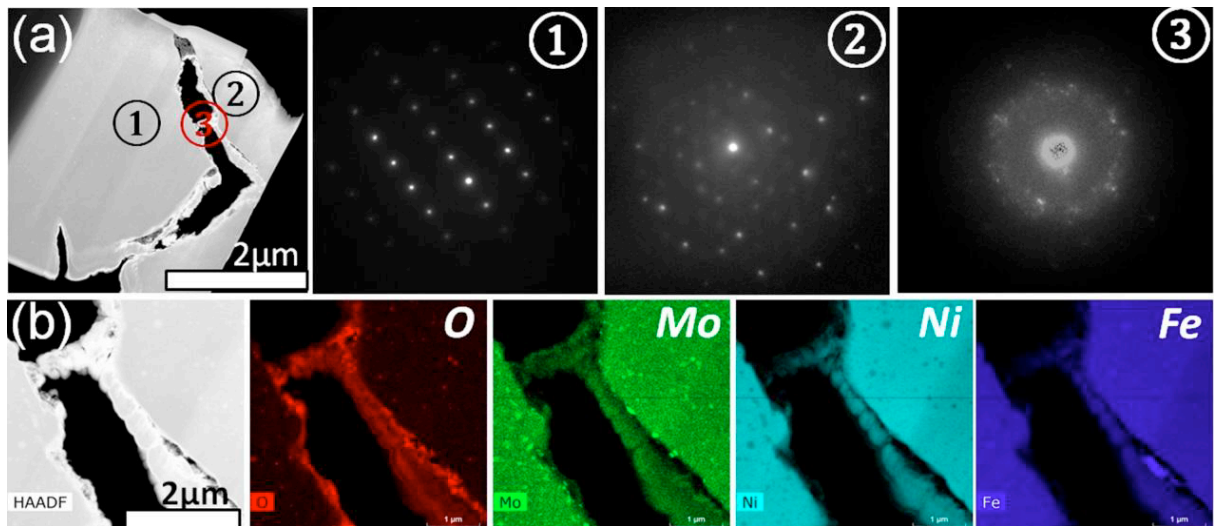
Figure 6: The TEM image (6a) and corresponding electron diffractions marked in 6a. 6b is the detailed microstructure of the crack shown in 5c and its elemental mapping.
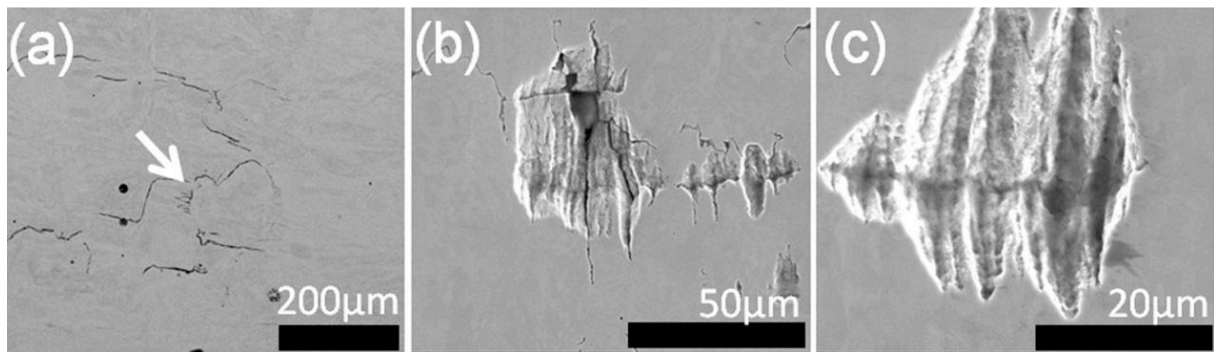
Figure 7: Type II crack with different magnification, the inner part of the crack was pull-out during polishing, leaving a dendrite structure.
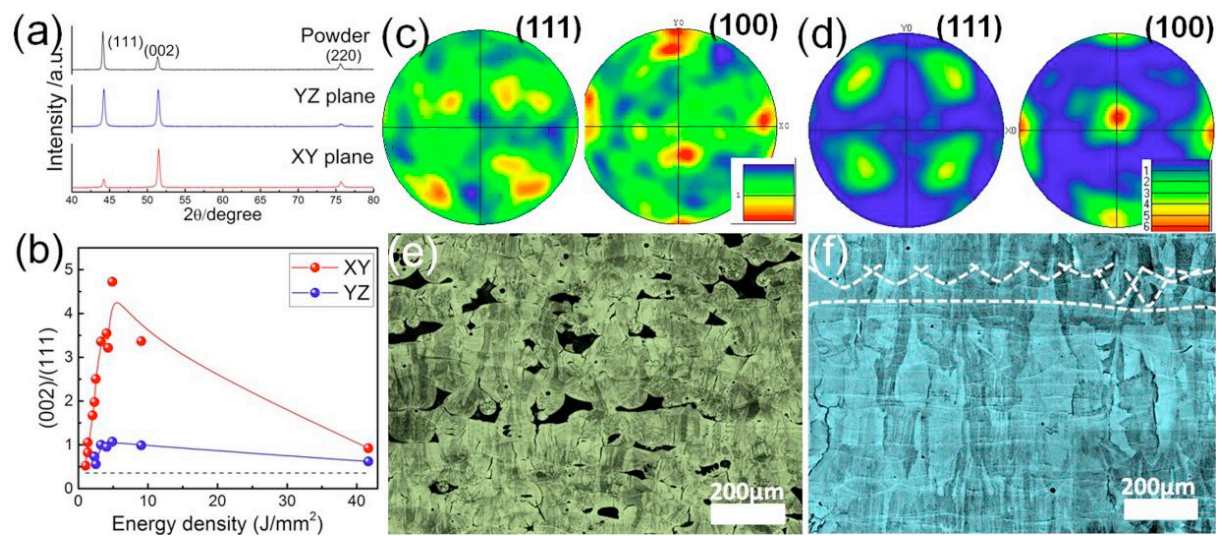
Figure 8: XRD patterns collected from the starting permalloy-80 powder, the top surface (XY) and side surface (YZ) of permalloy-80 (8a) built at an energy density of 4.89 J/mm^2. 8b shows the XRD intensity ratio between (001) and (111) peaks of permalloy-80 as a function of energy density. 8e and 8f are optical images collected from polished and etched surface of LPBFed permalloy-80 built at an energy density of 1.36 J/mm^2 (LE, 8e) and 4.89 J/mm^2 (HE, 8f). The (111) and (100) pole figures of 8e and 8f are shown in 8c and 8d, respectively.
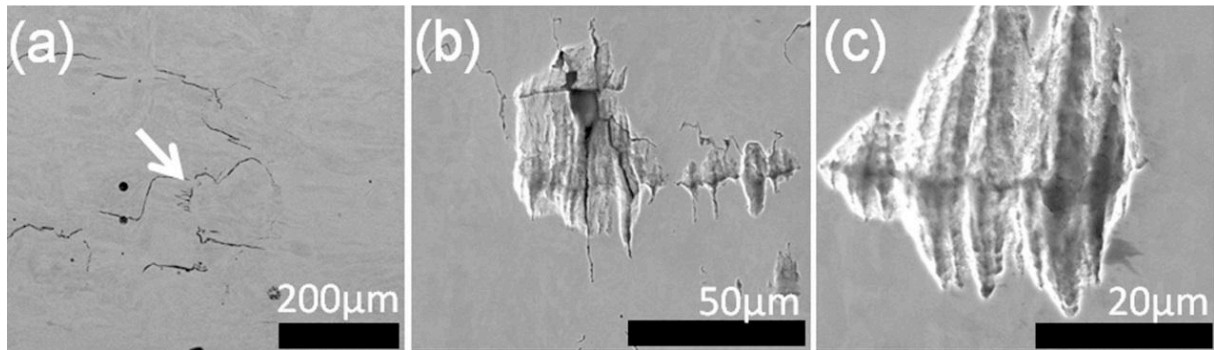

Figure 9: The density and coercivity of as-LPBFed permalloy-80 as a function of energy densities (9a). A mismatch between grain growth and orientated direction for the magnetic domains (as arrowed) could clearly be recognized from a comparison between the topography view collected by AFM (9b) and MFM view (9c). HE was used for AFM and MFM observation. An arrow highlighted the domain passing through a grain boundary is shown in 9c.
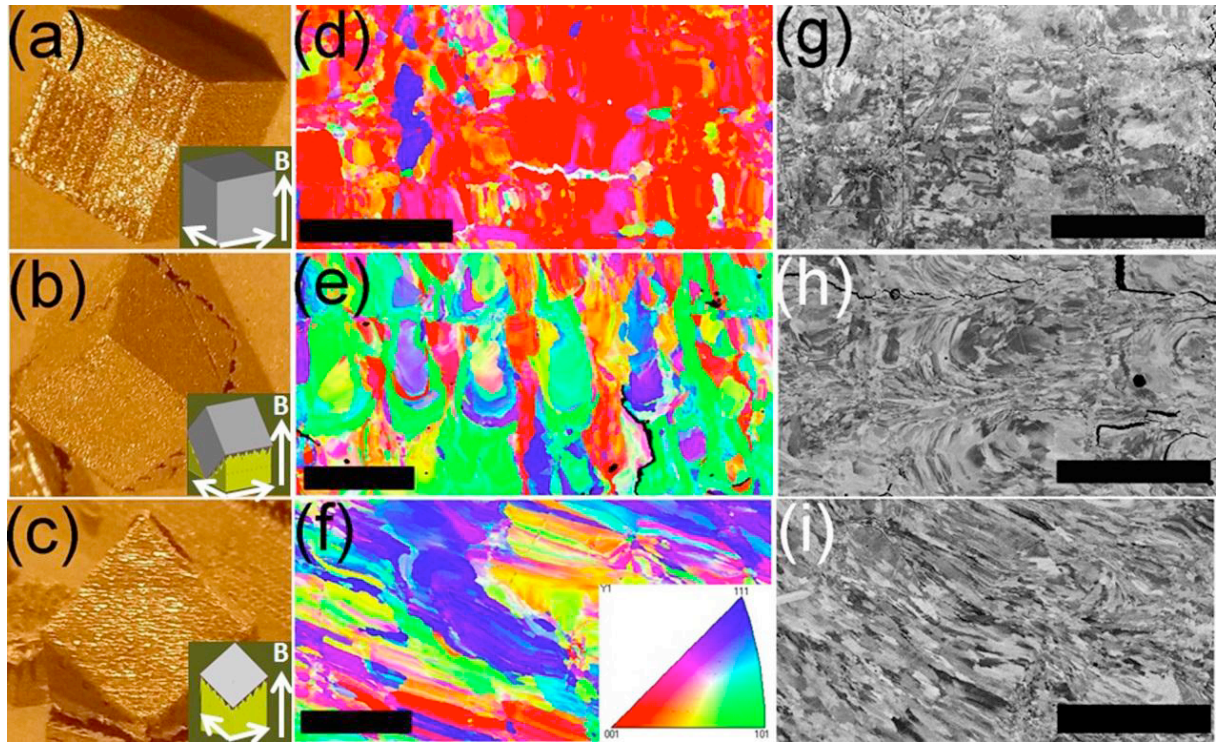
Figure 10: The photograph, EBSD map and SEM images of permalloy-80 built at different geometries. 10a, d and g are <100> geometry; 10b,e and h are <110> geometry, while 10c,f and I are designed according to <111> geometry. All the building directions are normal to the substrate with the coordination schematically shown in 10a, 10b and 10c. All the scale bars in Figure 10 represent 200μm.
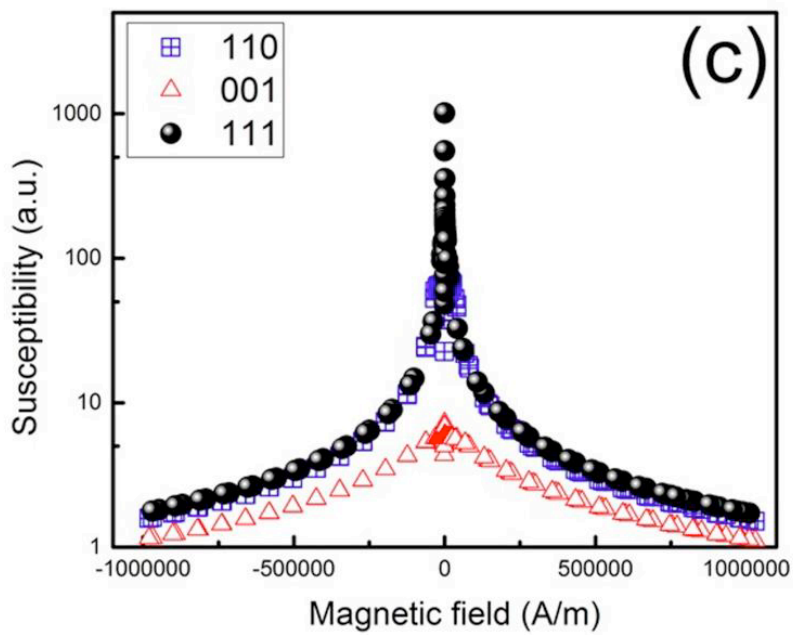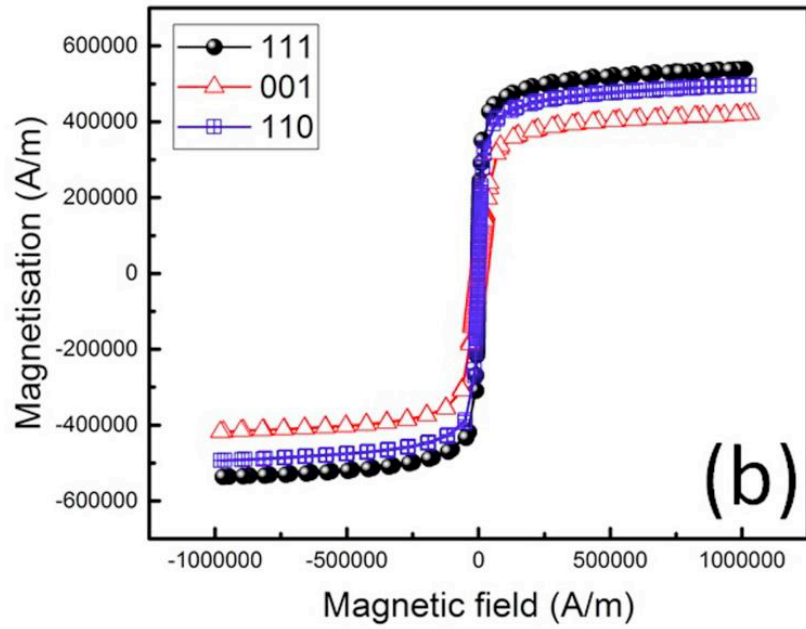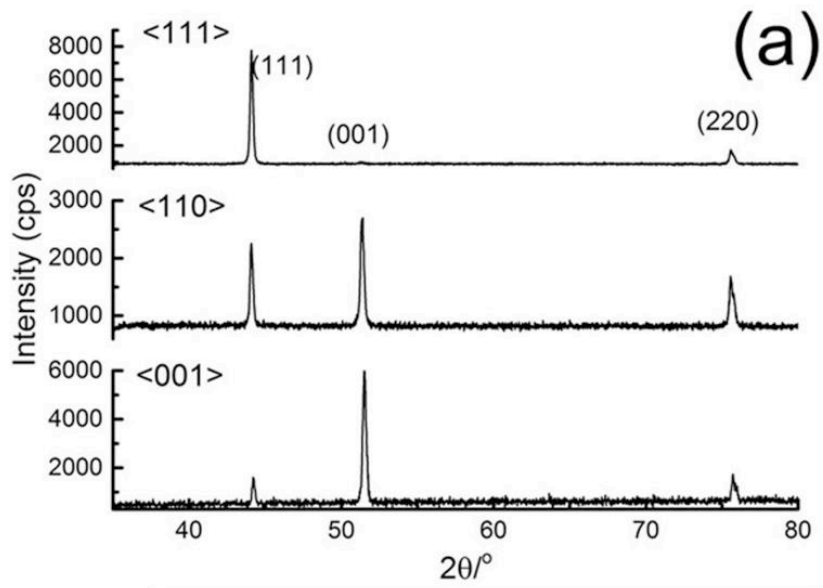
Figure 11: (a) XRD diffraction patterns for the sample in 10a-c. Hysteresis loops of the as fabricated permalloy-80 samples with different geometries (11b), 11c presents the calculated magnetic susceptibility of different samples as a function of the magnetic field.

Table captions

Table 1: Detailed scanning parameters for design of experiment.

Sample code	Energy density (J/m^2)	Laser power (W)	Scan speed (mm/sec)	Scan spacing (a1)
	0.64	160.81	3209.48	0.52
	0.81	100.00	2050.00	0.40
	1.04	250.00	4000.00	0.40
	1.19	160.81	3209.48	0.28
	1.36	250.00	2050.00	0.60
LE	1.36	339.19	3209.48	0.52
	2.03	250.00	2050.00	0.40
	2.32	160.81	890.52	0.52
	2.51	339.19	3209.48	0.28
	3.25	400.00	2050.00	0.40
	4.07	250.00	2050.00	0.20
	4.28	160.81	890.52	0.28
HE	4.89	339.19	890.52	0.52
	9.03	339.19	890.52	0.28
	41.67	250.00	100.00	0.40